



Two-dimensional temperature and carbon dioxide concentration profiles in atmospheric laminar diffusion flames measured by mid-infrared direct absorption spectroscopy at 4.2 μm

Xunchen Liu¹ · Guoyong Zhang¹ · Yan Huang¹ · Yizun Wang¹ · Fei Qi¹

Received: 15 October 2017 / Accepted: 19 March 2018 / Published online: 23 March 2018
© Springer-Verlag GmbH Germany, part of Springer Nature 2018

Abstract

We present a multi-line flame thermometry technique based on mid-infrared direct absorption spectroscopy of carbon dioxide at its ν_3 fundamental around 4.2 μm that is particularly suitable for sooting flames. Temperature and concentration profiles of gas phase molecules in a flame are important characteristics to understand its flame structure and combustion chemistry. One of the standard laboratory flames to analyze polycyclic aromatic hydrocarbons (PAH) and soot formation is laminar non-premixed co-flow flame, but PAH and soot introduce artifact to most non-contact optical measurements. Here we report an accurate diagnostic method of the temperature and concentration profiles of CO_2 in ethylene diffusion flames by measuring its ν_3 vibrational fundamental. An interband cascade laser was used to probe the R-branch bandhead at 4.2 μm , which is highly sensitive to temperature change, free from soot interference and ambient background. Calibration measurement was carried out both in a low-pressure Herriott cell and an atmospheric pressure tube furnace up to 1550 K to obtain spectroscopic parameters for high-temperature spectra. In our co-flow flame measurement, two-dimensional line-of-sight optical depth of an ethylene/ N_2 laminar sooting flame was recorded by dual-beam absorption scheme. The axially symmetrical attenuation coefficient profile of CO_2 in the co-flow flame was reconstructed from the optical depth by Abel inversion. Spatially resolved flame temperature and in situ CO_2 volume fraction profiles were derived from the calibrated CO_2 spectroscopic parameters and compared with temperature profiles measured by two-line atomic fluorescence.

1 Introduction

Soot formation from combustion intermediates under fuel-rich condition reduces heat generation, limits the combustor performance, and is one of the major environmental concerns of combustors. The complicated process involves PAH inception, followed by coagulation and condensation to form soot particles, and subsequent soot particle oxidation [1, 2]. One standard type of laboratory flame to study soot formation in mixing controlled combustion processes is co-flow laminar diffusion flame which has been characterized in great detail by comprehensive application of accurate

diagnostics tools [3, 4]. With ethylene as the most common fuel, Santoro-type coannular burner has been used to study particle formation, growth, and burnout in diffusion flames under atmospheric pressure conditions [5–8]. Factors that affect soot formation such as hydrogen and nitrogen additions [9, 10] and reaction kinetics have been studied [11].

In these studies, flame structure and temperature appeared to be the most significant factors to determine the propensity to form soot in diffusion-controlled combustion systems. Therefore, spatially resolved temperature measurements in sooting flames are essential for improving the overall understanding of soot formation and oxidation, as well as combustion kinetic modeling. Besides important flame parameters such as flow field and soot properties, high-fidelity flame temperature measurements are rare. Currently, temperature profile measurement of co-flow flames includes rapid insertion thermocouple technique for gas phase temperature [5], color ratio pyrometric measurements for soot temperature [12–14], and multi-color pyrometry imaging of flame spontaneous emission. However, there is strong evidence that the soot temperature differs from the gas phase temperature

This article is part of the topical collection “Mid-infrared and THz Laser Sources and Applications” guest edited by Wei Ren, Paolo De Natale and Gerard Wysocki.

✉ Xunchen Liu
liuxunchen@sjtu.edu.cn

¹ School of Mechanical Engineering, Shanghai Jiao Tong University, 800 DongChuan Rd., Shanghai, China

over large regions of the flame. Another widely used non-contact gas phase thermometry technique for co-flow flame measurement is coherent anti-Stokes Raman spectroscopy (CARS) [15–17]. Kliewer et al. used a time-resolved picosecond laser to successfully suppress both non-resonant background and smeared vibrational CARS signal in a sooting Santoro-type co-flow burner [18]. Besides complicated CARS system, by far the most practical 2D thermometry technique is two-line atomic fluorescence (TLAF). However, possible interference from the fluorescence from PAH, laser-induced incandescence (LII) and elastic scattering from soot particles must be eliminated and one usually needs to calibrate the measured intensity ratio with thermocouple measurements [19]. TLAF thermometry was successfully applied by Sun et al. to investigate two series of laminar co-flow ethylene/hydrogen/nitrogen flames, aiming to separate the complementary effects of H₂ or N₂ addition and the exit flow velocity (strain rate), respectively [20]. The quantitative trend of co-flow sooting flame temperature involves increase with fuel flow rate, maximum along the radial direction at the flame front, and decreases higher in the flame due to increased radiative heat transfer from soot.

Another widely used diagnostic technique for diffusion flame measurement is light extinction method. In the infrared region, tunable diode laser absorption spectroscopy (TDLAS) is a non-intrusive, absolute and accurate method to measure small to medium size gas phase molecules. In the near-IR region, spatially resolved concentration and gas temperature of water molecules have been measured in premixed flames [21–25]. In an atmospheric laminar counter-flow diffusion flames study, N₂-CARS thermometry was used to determine flame temperature in priori for spatially resolved CO concentration profiles at 2.3 μm [26]. The 1.5 μm ($2\nu_1 + 2\nu_2 + \nu_3$) and 2.0 μm ($\nu_1 + 2\nu_2 + \nu_3$) overtone spectral region have been used for remote-sensing measurements of CO₂ at low to ambient temperature with percent level intensity uncertainty. At low pressure, high-temperature gas sample of carbon dioxide has been studied using high-temperature absorption cell [27] with medium-resolution [28, 29] and high-resolution FTIR instrument [30]. The 2 μm near-IR rovibrational transitions have been investigated for in situ combustion diagnostic studies [31–36]. For example, Cai et al. have demonstrated simultaneous measurement of temperature and CO₂ concentration in a static calibration cell and on a test burner using a diode laser at 2.0 μm [37]. Farooq et al. developed a two-line thermometry method at 2.7 μm ($\nu_1 + \nu_3$) [38, 39] with two DFB lasers at 3645 and 3633 cm⁻¹ accessing the *P*(70) and *R*(28) transitions of the $\nu_1 + \nu_3$ band, respectively.

The mid-infrared spectral region covers molecular fundamental bands with large absorption coefficients and offers unique opportunity for highly accurate measurement of flame temperature and CO₂ concentration in combustion

system. Recently, shock tube and flame temperature measurement using quantum cascade (QC) lasers at this wavelength have been reported using direct absorption method. Nau et al. used a QC laser operated in intra-pulsed spectroscopy mode at 4.5 μm to measure the fundamental absorption band of CO and CO₂ molecules [40] for low-pressure propane/oxygen-premixed McKenna flat flames. But *P*-branch of CO₂ and *R*-branch of CO interfere at 4.5 μm in this measurement. On the contrary, the *R*-branch of the ν_3 asymmetric stretching fundamental band of CO₂ at 4.2 μm is isolated from interfering combustion species such as water and carbon monoxide. The HITEMP simulation of ν_3 fundamental absorption coefficients at 1500 K in Fig. 1a shows that the high-frequency end of the *R* branch is particularly interesting because the only interfering hot band here is the first bending hot band of ν_3 mode. Numerous hot bands that would interfere with the ν_3 fundamental at elevated temperature progress to the low-frequency end, making the region further

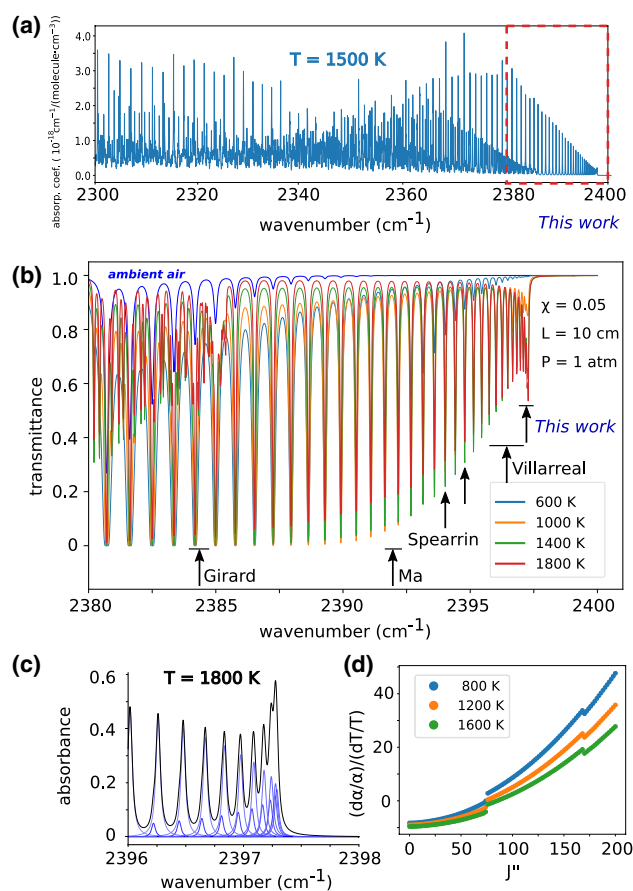


Fig. 1 Unique feature of the R-branch band head making it suitable for combustion diagnostics: **a** simulation of CO₂ absorption coefficient for the fundamental band at 1500 K. **b** Simulation of transmittance spectra for the far wing of *R*-branch under typical combustion diagnostic application. **c** Zoom-in view of the absorbance simulation of band head region. **d** Temperature sensitivity of the R-branch transitions

to the red unresolvable under combustion environment due to multiple hot band transitions.

As indicated in Fig. 1b, using two continuous wave mode QC laser, Spearrin et al. reported a two-line thermometry technique that uses $R(96)$ of ν_3 band at 2395 cm^{-1} paired with $R(28)$ line of $\nu_1+\nu_3$ band at 3633 cm^{-1} [41]. The temperature insensitive $R(92)$ transition of ν_3 band at 2394 cm^{-1} was also used for precise CO_2 measurement [42]. Using a wide-range external cavity QC laser, Wu et al. reported a similar two-line thermometry technique that utilizes $R(96)$ and $R(74)$ transition pair which are 5 cm^{-1} apart and required the laser to be operated at two separate positions [43]. A two-line thermometry technique that utilizes adjacent transitions that can be covered within a single laser scan was recently reported by Girard et al. [44]. A distributed feedback interband cascade (IC) laser centered at 2384 cm^{-1} was used to cover $R(58)$ transition of the ν_3 fundamental and $R(105)/R(106)$ combination of the weaker band head of the first bending hot band of ν_3 mode. Ma et al. also demonstrated sensitive CO_2 detection using a similar IC laser that covers the adjacent $R(80)$ and $R(82)$ transitions of ν_3 fundamental at 2392 cm^{-1} [45]. In these two studies, measurements were made of premixed laminar flame under low and ambient pressure. Actually, Villarreal and Varghese have measured CO^{-2} temperature and concentration profiles of a McKenna flat-flame by investigating the band head at the high-frequency end of the of R-branch using a cryogenically cooled lead salt laser [46]. Assuming axisymmetric distributions, Abel inversion of line-of-sight absorption signal at each laser frequency was reassembled to obtain tomographic reconstructed high-resolution absorption spectra of the radial node. Tomographic reconstruction of line-of-sight absorption measurement was frequently reported in studies of one-dimensional planar premixed flame on McKenna burners [22, 24, 46] or laminar 2D diffusion flame [47], but little work has been reported for co-flow diffusion flames.

There are several advantages of choosing the band head region for combustion diagnostics of CO_2 in the flame environment. First of all, the band head region is free from the background ambient CO_2 absorption. With large absorption coefficients in the mid-infrared region, CO_2 in ambient air would generate significant background absorption in a typical free space coupling experimental configuration. Figure 1b shows simulation of 200 cm ambient air absorption with 400 ppm volume fraction. It is obvious that background absorption has to be considered to the red of 2390 cm^{-1} . At the band head region, however, the ambient air background is negligible. This is a valuable feature when the TDLAS sensors have to be placed to a distance from the target in combustion diagnostics applications. A zero background absorption beyond the outermost projection radius is also prerequisite for Abel inversion of the axisymmetric co-flow flame, while non-zero signals beyond the transformation

size needs to be removed before performing any tomography reconstruction [48].

The second advantage is the fact that the band head region is not easily saturated in practical application. Considering a typical real field application of 10-cm-long path flame with 5% CO_2 . As shown in Fig. 1b, simulation of the transmittance data at 600, 1000, 1400, and 1800 K indicate that the CO_2 absorption would almost saturate the signal at peak positions used by Girard et al. and Ma et al., making the obtained absorbance value in the non-linear region. Therefore, the transmitted laser power around the band head region is higher compared to the almost absorption saturated low wavenumber region.

Further, the band head region has very high temperature sensitivity at elevated temperature. The band head intensity would increase at high temperature due to the increase of absorption coefficients of high J transitions which have positive temperature sensitivity. Simulation of the band head absorbance at 1800 K is shown in Fig. 1c. The $R(120/122/124)$ and $R(118/126)$ transitions are overlapped to form peaks with increased absorbance, and the further high J transitions are shown as asymmetric shoulders. Figure 1d shows the calculated temperature sensitivity of the absorption coefficients of the ν_3 R-branch transitions at 800, 1200, and 1600 K. Multiple data sources caused sporadic discontinuities at $R(75)$ and $R(175)$ of rovibrational lines. The high J transitions around the band head have large positive temperature sensitivity, i.e., absorption coefficients increase with temperature. This unique feature, combined with the absence of background absorption, making the ν_3 band head very suitable for combustion diagnostics application: the TDLAS sensors can be placed away from the flame and the line-of-sight measurement would only have high temperature CO_2 absorption but no ambient background signal.

One more advantage of using the band head transitions is the fitting of several simultaneously measured transitions improves accuracy [46]. The multi-spectral absorption spectroscopy method is also favored in tomographic imaging [49]. Therefore, the reason is sufficient for another study to develop a TDLAS sensor with the newly available IC laser to target the multiple peaks at band head that are free from ambient background and have positive temperature sensitivities. In this study, we utilize this unique feature to develop an in situ CO_2 thermometry sensor for combustion diagnostic of a typical co-flow laminar diffusion flame.

But the challenge associated with the band head peak thermometry is also obvious: the highly conjugated band head transitions are overlapped and not well separated. Nine overlapping peaks from $R(114)$ to $R(130)$ form four apparent peaks above 2397 cm^{-1} that cannot be simply fitted by four transitions. The overlapping peaks are highly sensitive to tiny errors in the line position, line strength and broadening

parameters. Therefore, calibration measurement at high temperature are a priori for diagnostic applications.

In this paper, we report 2D measurement of temperature and CO₂ concentration profiles of a laminar co-flow sooting flame obtained by single path direct absorption spectroscopy at the band head region of ν_3 fundamental at 2397 cm⁻¹. To convert the path integrated absorption signal to spacial resolved absorption coefficients, inverse Abel transformation was performed with Tikhonov regularization method.

2 Experimental method and model

2.1 Experimental setup

The schematic experimental setup is depicted in Fig. 2. To reduce laser power noise and following noise amplification in ill-conditioned Abel inversion, we used dual-beam absorption scheme to reduce the laser intensity fluctuation. The laser beam from a distributed feedback inter-band cascade laser centered at 4172 nm (Nanoplus, Germany) was divided to three beams: the probe and reference beams to measure flame absorption and a solid germanium Fabry–Perot etalon for wavelength tuning calibration. The length of the Ge etalon was 80 mm and the free spectral range of the etalon is 0.0153 cm⁻¹ at this wavelength. The laser injection current and temperature was controlled by a laser diode controller (LDTC0520, Wavelength Electronics, USA). The injection current was modulated by triangle waveform from a function generator (Tektronix AFG3022C) to scan the laser wavelength and the laser

temperature was tuned to the optimal scan range to cover the *R*-branch band head region. The scanned laser intensities were measured by three thermoelectrically cooled mercury cadmium telluride (MCT) photovoltaic detectors (PVI-2TE, Vigo System, Poland).

Measurement of the laser beam propagated through a flame faces two problems. One is thermal deflection of the beam from its axis, induced by sharp temperature gradients at the edge of the diffusion flame [50, 51]. To minimize the thermal gradient effects, a 1-inch silicon positive meniscus lens was closely placed behind the flame to focus the laser beam to the detector. Measurement of the infrared absorption spectra of high-temperature object such as flames also faces the problem of large thermal radiation from flame. To probe the small transmitted signal change, usually a narrow band filter has to be used. But such filters are not always readily available and cannot complete block thermal background in practical applications with the presence of strong thermal radiation. Instead, we restricted the preamplifier bandwidth of the MCT detectors to 100 Hz–5 MHz, so that the slow time variant thermal radiation acted as low-frequency component and was filtered out. We could thus improve the linear behavior of the MCT detector in the presence of incident radiation intensity. The amplified voltage signal was then digitized by a 25 MS/s 16 bit PCI digitizer (Gage Applied, OVE-844, USA).

To generate the co-flow laminar diffusion flames, we used a Santoro-type burner schematically shown in Fig. 2. Details of the burner has been reported elsewhere [11]. Flow of ethylene (99.9%, Chunyu, Shanghai) and nitrogen (99.9% purity, Chunyu, Shanghai) from gas cylinder mixed in the center fuel tube and the flow of the co-flow air from a compressor were controlled by mass flow meters (GM50A, MKS, USA and SevenStar, Beijing). The burner was operated under open atmospheric conditions. The burner was mounted on a vertical and a horizontal step motor stage (PSA50/150-11-x, Zolix, Beijing) and moved in the 2D plane that is perpendicular to the laser beam so that line-of-sight measurements of the diffusion flame can be performed at different heights above the burner (HAB) and radial position. Two sooting laminar diffusion flames were studied to compare with reported laminar sooting flame II-6 and II-4 in Ref. [20]. The volumetric fraction of C₂H₄/N₂ was controlled at 60/40% and 80/20%, respectively, while the cold gas flow velocity was fixed at 5 cm/s. Although the diameter of the burner under investigation is 0.5 mm smaller than the Adelaide burner, the laminar co-flow diffusion flames stabilized on the fuel tube with the same fuel percentage and exit flow velocities are very similar in terms of flame structure and flame height. Therefore, comparison of flame temperature profiles can be made between the current measurement and those of Sun et. al. [20].

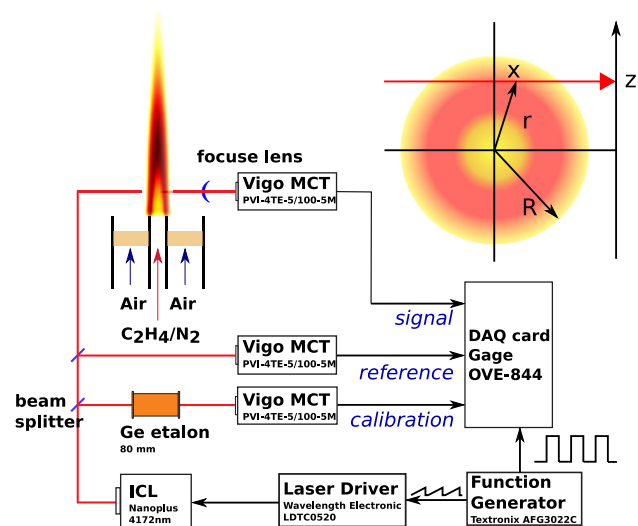


Fig. 2 Dual-beam absorption experimental setup and geometry of the axisymmetric co-flow flame. Flow of fuel tube consisted of 60% C₂H₄ with 40% N₂ with 5 cm/s exit speed and the co-flow air exit speed was 15 cm/s

2.2 Model

Assuming the co-flow flame is axisymmetric, Abel inversions was used to obtain the exact attenuation coefficients at each wavenumber through parallel integrated absorption measurements as a function of height from the burner exit. The geometry of an axisymmetric co-flow flame is shown in Fig. 2. The path integrated fractional absorption of the incident laser intensity I_0 is related to temperature, pressure, and number density of the CO₂ molecules:

$$-\frac{I}{I_0} = \exp[\tau] = \exp\left[\int_l \mu(r) dl\right] = \exp\left[\int_l [X] k(\nu, T, p) dl\right] \tag{1}$$

where τ is the integrated optical depth; $[X]$ is the volume number density of CO₂ (molecule per cm³); $k(\nu, T, p)$ is the monochromatic absorption coefficient (cm⁻¹ per molecule per cm³) at wave number ν , which is the product of the transition line strength $S(\nu, T)$ and the transition line-shape function $f(\nu; \nu_0, T, p)$. In this study, we use Voigt line-shape function $f_{\text{Voigt}}(\nu; \nu_0, T, p)$ which is the convolution of temperature-dependent Gaussian type Doppler broadening lineshape $f_D(\sigma)$ and Lorentzian type pressure broadening lineshape $f_L(\gamma)$. The Voigt line shape is evaluated as the real part of the Faddeeva function $w(z)$: [52]

$$f_{\text{Voigt}}(\nu; \nu_0, T, p) = \frac{\text{Re}\left[w\left(\frac{\nu+i\gamma}{\sigma\sqrt{2}}\right)\right]}{\sigma\sqrt{2\pi}} \tag{2}$$

The path integrated optical depth τ measured at lateral positions z of a flame with radius R is related to the attenuation coefficients $\mu(r)$ through Abel transformation (Fig. 2):

$$\tau = 2 \int_0^{\sqrt{R^2-z^2}} \mu(r) dx = 2 \int_z^R \mu(r) \frac{r}{\sqrt{r^2-z^2}} dr \tag{3}$$

There are various algorithms for Abel transformation, such as onion-peeling, Abel-three-points [53], Fourier–Hankel, and Gaussian basis-set expansion [54]. The standard transformation can be written as:

$$\mathbf{A} \mathbf{M} = \mathbf{T} \tag{4}$$

in which \mathbf{A} is the projection matrix, \mathbf{M} is the local attenuation coefficients array and \mathbf{T} is the discretized path integrated optical depth, both of dimension N . In this study, we used Abel-three-point method and Tikhonov regularization to address the inherent ill-conditioned nature of Abel inversion, by an additional set of equations:

$$\lambda \mathbf{L} \mathbf{M} = 0 \tag{5}$$

in which λ is regularization parameter range from 0 to 1; \mathbf{L} is the gradient operator to ensure that \mathbf{M} is smooth, i.e.,

$$\mathbf{L} = \begin{bmatrix} 1 & -1 & 0 & \dots & 0 \\ 0 & 1 & -1 & \dots & \vdots \\ \vdots & \vdots & \ddots & \ddots & \vdots \\ 0 & 0 & \dots & 1 & -1 \end{bmatrix}_{N-1 \times N} \tag{6}$$

The over-determined local attenuation coefficients array \mathbf{M} can then be determined by least-squares fitting of the following set of equations:

$$\begin{bmatrix} \mathbf{A} \\ \lambda \mathbf{L} \end{bmatrix} \mathbf{M} = \begin{bmatrix} \mathbf{T} \\ 0 \end{bmatrix} \tag{7}$$

2.3 Calibration

In the high-temperature calibration process, a high-temperature static cell was developed, which consists of an 40-cm-long alumina (Al₂O₃) ceramic tube placed in a home-made three-stage high-temperature oven. Temperature control of the oven is similar to the design of a high-temperature flow reactor pyrolysis apparatus [55]. The actual temperature value (T_{tube}) inside the ceramic tube was measured by a B-type thermocouple (Pt30Rh-Pt6Rh) with the thermocouple’s bead placed along the longitudinal axis of the ceramic tube using a ceramic rod. Figure 3 shows the temperature profiles measured at different oven temperatures after thermal equilibrium have been reached. A 20-cm-long section with uniform temperature was achieved by adjusting the ratio of the three independently controlled heating section temperatures. Two 24-cm-long sapphire rods with wedged end faces were used to fill the low-temperature sections of the ceramic tube and provide sealing at the cold end of the ceramic tube. The central uniform high-temperature stage was purged by CO₂/N₂ mixture gas under interrogation. Note that the transmittance of sapphire at 4.2 μm decreases as temperature increases. Above 1600 K the weak transmitted

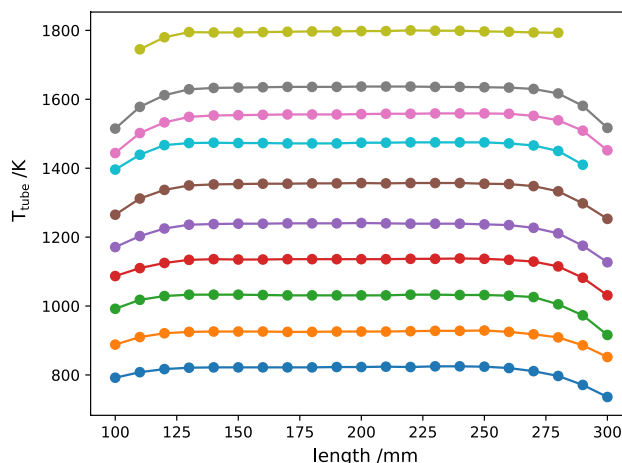


Fig. 3 Centerline temperature profiles of the calibration temperatures measured by the B-type thermocouple

laser light has prohibited respective measurements. Since the CO₂ band head line strength is weak under 500 °C, we have measured calibration spectra from 800 to 1550 K. Typical measurement series were performed at thermal equilibrium conditions with volume fraction of CO₂ diluted in nitrogen ranging from 2.0 to 10.0%, controlled by the flow rate of two MKS mass flow meters.

To further confirm the transition wave number of the band head region, we measured the absorption spectrum of low-pressure CO₂ sample at high temperature. A Herriott type multipass cell (Thorlab CM508-200/EH4) was used to increase the absorption path. The multipass cavity consisted of two gold-coated 2-inch concave mirrors, with one has an off-axis hole, placed in low-pressure chamber heated to around 800 °K and maintained at 1 Torr to reduce the pressure broadening.

The measured band head spectra of low-pressure CO₂ in a Herriott cell heated around 500 °C are shown in Fig. 4. Figure 4a, c shows the laser ramp of etalon and Herriott cell transmission measured as raw signal. The etalon and absorption peaks are then used to calibrate the laser scan. The calibrated etalon and background subtracted Herriott cell absorption spectrum are shown in Fig. 4b, d. Simulation of the transmission spectrum using HITEMP database [56] is also shown in Fig. 4d. HITEMP database can perfectly simulate the low-pressure spectrum of the band head transitions from the ν_3 fundamental. An extra P(36) line from the $10^0 1^1 \leftarrow 10^0 0^2$ band is visible from the Herriott cell measurement, but this line is very weak at flame temperature. The linewidth of the well-isolated transitions would increase upon high pressure, so they will merge to broad peaks under ambient pressure and the weak high J transitions would be identified as asymmetric shoulders.

The furnace calibration spectra are measured from 800 to 1550 K with CO₂ volume fraction range from 2.0 to 10.0% to

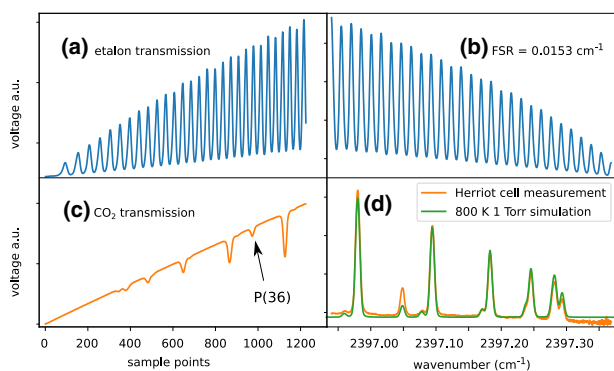


Fig. 4 Herriott cell measurement of the band head spectrum at low pressure. **a** Direct etalon transmittance, **b** calibrated etalon transmittance, **c** raw multipass cell transmittance of CO₂, **d** measured and simulated CO₂ spectra. Note the extra transition belongs to $10^0 1^1 \leftarrow 10^0 0^2$ band

mimic the co-flow flame condition at ambient pressure. An example set of measured optical depth of CO₂ at 1200 °C is shown in Fig. 5a, together with the measured low-pressure spectrum with reduced Doppler broadening. Good linear relationship is found between the CO₂ volume fraction and the measured optical depth. The insert of Fig. 5a shows the least-square fit of the peak height at 2397.1 cm⁻¹ and CO₂ fraction, which confirms that the band head thermometry present in this paper is in the linear absorption region and would not cause absorption saturation. The measured optical depths are then converted to absorption coefficients from 800 to 1550 K shown in Fig. 5b, which demonstrate the unique feature of positive temperature sensitivity in the band head region, i.e., the absorption coefficients increase upon temperature rises. An apparent underestimation of the line strength is found for the HITEMP simulation compared to the experimental calibration spectra at high temperature. At the very end of the band head where R(120/122/124) peaks overlap, the HITEMP simulation obviously missed the sharp band head in the measurement, which might be due to collisional narrowing effect that was not included in the Voigt line shape function.

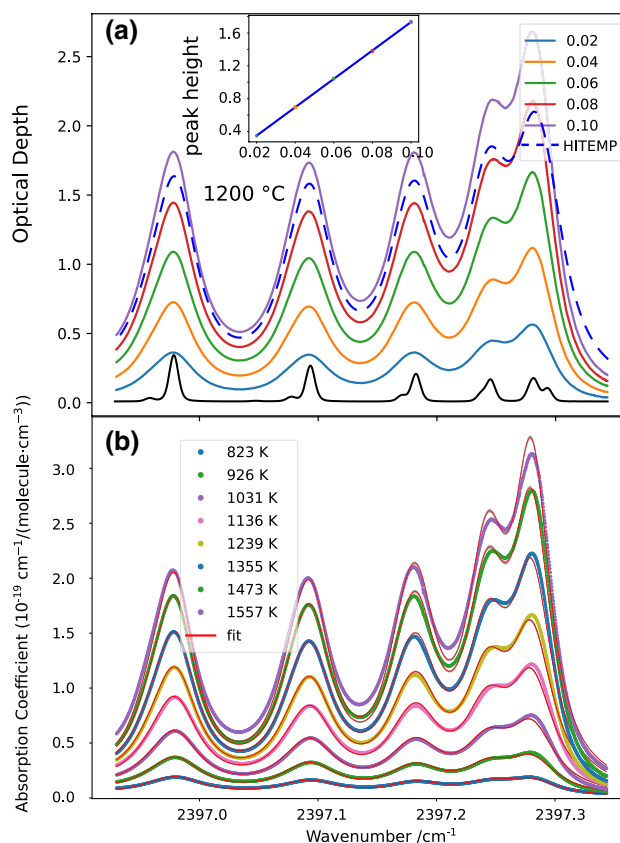


Fig. 5 Tube furnace calibration spectra. **a** Experimental and HITEMP-simulated optical depth with different CO₂ volume fraction at 1200 °C, **b** multi-spectra fit of the experimental absorption coefficients range from 500 to 1000 °C

We then performed Levenberg–Marquardt multi-spectra least-square fit of the high-temperature calibration spectra using the same strategy as Villarreal et al. [46], in which low J transitions from HITRAN database starting from 2390 cm^{-1} were included to provide the broadened wings, with collision widths and pressure induced shifts varied. Both line position and line strength of all transitions are fixed. Ambient pressure was fixed to 1 atm in all the fitting. But there is apparent discrepancy around the band head peak at $2397.25\text{--}2397.30\text{ cm}^{-1}$ due to collisional narrowing of the overlapped transitions. The multiple W-shape residues indicate further improvement with variable pressure calibration measurements and lineshape model beyond Voigt lineshape such as Hartmann–Tran profile [57] will be needed. The line position, line strength, and line broadening parameters are shown in Table 1.

Generally speaking, the fitted spectra are in good agreements with experimental ones as plotted in Fig. 5b. The

Table 1 Adjusted line position, strength, and broadening parameters

	ν	S	γ_{air}	n_{air}	E
R110	2396.979410	1.626E-27	0.0599	0.67	4917.2744
R112	2397.094125	7.045E-28	0.0600	0.67	5092.8770
R114	2397.182454	3.006E-28	0.0563	0.67	5271.5171
R116	2397.245227	1.264E-28	0.0543	0.68	5453.1924
R118	2397.282072	5.233E-29	0.0540	0.68	5637.9004
R120	2397.293041	2.135E-29	0.0537	0.68	5825.6372
R122	2397.278121	8.577E-30	0.0535	0.68	6016.3999
R124	2397.237297	3.396E-30	0.0532	0.69	6210.1855
R126	2397.170557	1.324E-30	0.0548	0.69	6406.9912
R128	2397.078100	4.968E-31	0.0508	0.58	6606.8131
R130	2396.959430	1.878E-31	0.0502	0.58	6809.6483

obtained temperatures from the least-square fitting T_{fit} are then calibrated to the actual gas temperature T_{tube} using the first-order polynomial as shown in Fig. 6a. The linear relationship was then used to calibrate the fitting temperature T_{fit} to obtain the final experimental temperature. The relative error was within 1.5% in the calibrated temperature range as shown in Fig. 6b. Thermometry measurement in complex environment with different broadening species such as in flames using the calibration results would suffer from larger uncertainties.

3 Results

In the co-flow diffusion flame measurement, the burner mounted on the 2D motor stage was scanned with 0.5-mm step in horizontal direction and 1-mm step in vertical direction. Fig. 7a shows the typical wavelength calibrated optical depth spectra between 2397.05 and 2397.35 cm^{-1} measured with dual-beam background subtraction at 0.5-mm step along the radial direction 20 mm above the burner. The scanned profiles of measured optical depth was then inversely transformed to local attenuation coefficient profiles at each wave number, resulting in the local attenuation coefficient spectra that is shown in Fig. 7b. In this process, small noise in the experimental measured spectra would be amplified by Abel inversion. First, numerically simulated forward projections in the presence of random noise was tested to validate the Abel inversion algorithm with Tikhonov regularization. The Abel-inverted radial profile clearly shows the CO_2 absorption signal gradually increases to maximum close to the edge of the flame and rapidly decreases to zero at the co-flow air, which is characteristic for diffusion-controlled laminar flames. CO_2 concentration and temperature

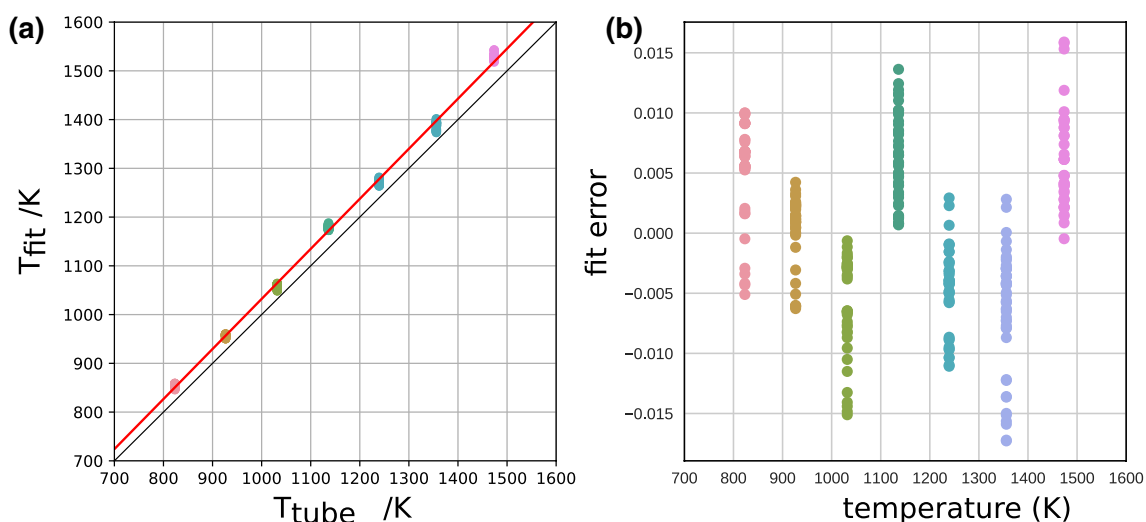


Fig. 6 **a** Non-linear least-square fitted temperature T_{fit} at different tube temperature T_{tube} ; **b** relative error of T_{fit} after calibration

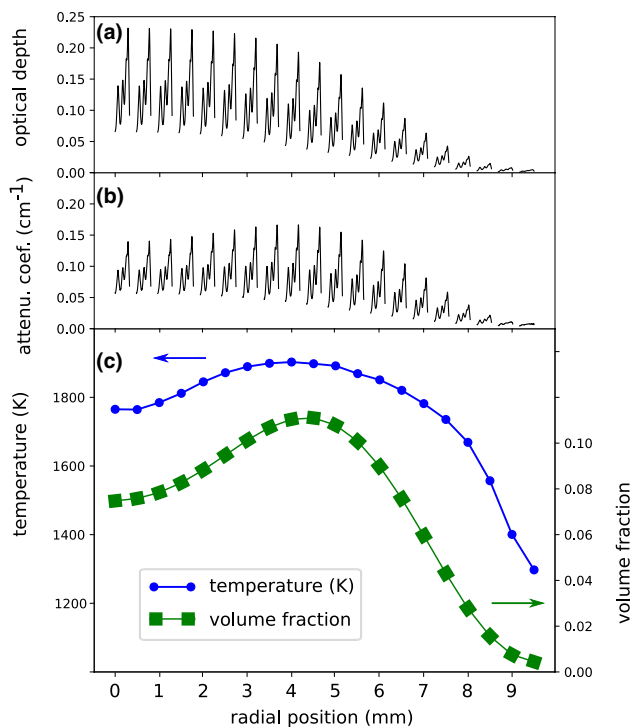


Fig. 7 Co-flow flame measurement data of 60% ethylene flame. **a** Line-of-sight optical depth measured at 20-mm HAB along the radial direction from parallel propagating laser beam; **b** local attenuation coefficients from Abel inversion of signal in **a**; **c** temperature and CO₂ volume fraction obtained from fitting of the attenuation coefficients

profiles were obtained from fitting of the local attenuation coefficients with spectra parameters determined from calibration in Table 1. The fitted temperatures have uncertainties mostly below 4% and the concentration uncertainties are around 10%.

Fitting of the attenuation coefficient spectral after Abel inversion was generally good. Figure 8 shows a typical non-linear fit of the local attenuation coefficient spectra. Figure 7c shows the temperature and volume fraction of CO₂ determined from local spectral fitting at 20 mm HAB. Here, it should be noted that scattering and absorption of laser light from soot particles leads to large background absorption shown in the measured attenuation coefficients. In the less than 1 cm⁻¹ region scanned, such apparent background absorption can be viewed as a wavelength-independent background absorption as shown in Fig. 8. Assuming that the optical properties of the soot and large hydrocarbons in the wavelength region we measured are the same as visible region, we estimated that the apparent volumetric soot concentration of the flames we measured was at ppm level, which was confirmed by the LII measurement [20].

Figure 9 shows the two-dimensional volume fraction and temperature profile of CO₂ obtained from tomographic reconstruction in this work and compares with

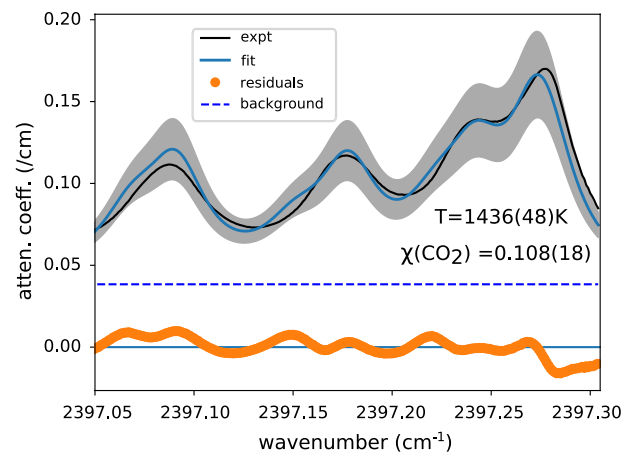


Fig. 8 A typical non-linear fit of local attenuation coefficient obtained from Abel inversion. Grey shade shows the 3σ uncertainty of fitting spectra

the temperature profile from TLAF measurement of laminar sooting flame II-6 and II-4 reported in reference [20]. Although the central fuel tube diameter and co-flow air velocity are different, the two flames have the same C₂H₄ fraction and flow velocity (5 cm/s) at the burner exit. Temperature profiles obtained from these two measurements show similar flame structure and quantitative agreement. It is demonstrated by the 2D volume fraction and temperature profiles that with more C₂H₄ fuel in the flow, the 80% flame is longer than the 60% flame, but with lower temperature profile due to higher amount of radiation loss from soot as

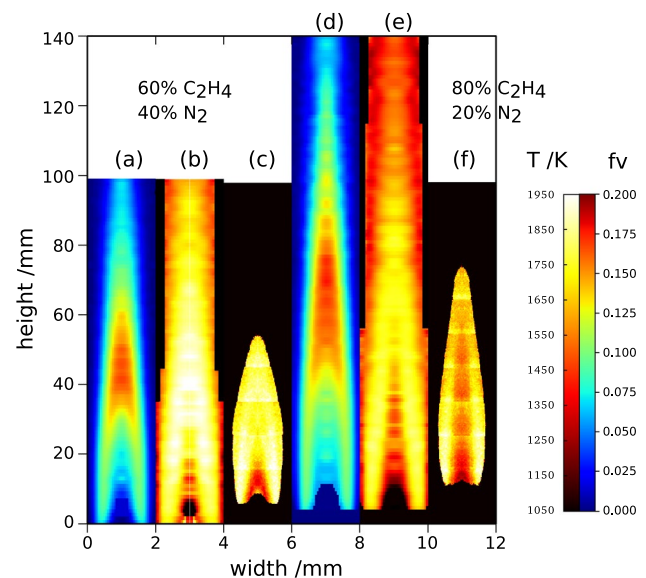


Fig. 9 Two-dimensional CO₂ volume fraction (**a**) and temperature (**b**) profiles obtained from non-linear fit of tomographic reconstructed attenuation coefficients. Also shown for comparison is **c** temperature profile obtained by TLAF measurement from reference [20]

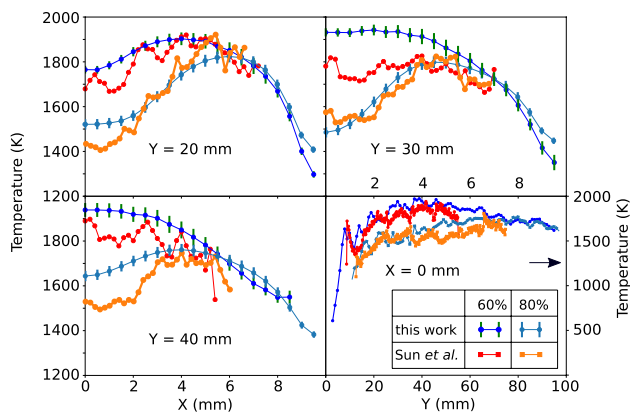


Fig. 10 Comparison of radial and axial flame temperature profiles obtained from tomographic reconstruction in this work and TLAF measurement from Ref. [20]

measured by laser-induced incandescence measurement in [20]. The good agreement of 2D temperature profiles demonstrate that the tomographic reconstruction based on band head multi-peak thermometry development in this paper can provide similar temperature measurement accuracy as fluorescence imaging method.

Figure 10 further compares temperature profiles of both 60 and 80% ethylene flames determined in this work with TLAF method in axial and radial directions, respectively. The TDLAS method agrees quantitatively with the TLAF method and shows high accuracy. It should also be noted that TDLAS method can provide flame temperature information immediately after the burner exit whereas TLAF method cannot, in which In atom signal only appears after the flame front.

4 Summary and conclusion

We have developed a TDLAS thermometry method based on direct absorption of the band head region of the $\text{CO}_2 \nu_3$ fundamental band. High J transitions range from R(114) to R(130) around $4.2 \mu\text{m}$ are overlapped in this region. The unique feature of ultralow background absorption and positive temperature sensitivity making this region excellent candidate for high-fidelity temperature measurement in combustion diagnostic application. A single head interband cascade laser was used to access the band with dual-beam absorption scheme to remove laser power instability, together with high-bandwidth MCT detectors to remove thermal background radiation. High-temperature calibration measurements were done in both low pressure and ambient pressure, to provide new spectroscopic parameters. Further improvement of the lineshape model beyond Voigt function is needed. Two-dimensional temperature and volume fraction profile

measurement of sooting laminar co-flow diffusion flame is demonstrated and compared with TLAF measurement, with good quantitative agreement.

Acknowledgements The authors thank Prof. Bin Zhou from Southeast University for helpful discussion about the interpretation of non-soot absorbance. Financial support by National Natural Science Foundation of China (51606123, 91541201) is gratefully acknowledged.

References

1. H. Richter, J.B. Howard, *Prog. Energy Combust. Sci.* **26**(4–6), 565 (2000)
2. C.S. McEnally, L.D. Pfefferle, A.M. Schaffer, M.B. Long, R.K. Mohammed, M.D. Smooke, M.B. Colkei, *Proc. Combust. Inst.* **28**(2), 2063 (2000)
3. S. Will, S. Schraml, A. Leipert, *Symp. Int. Combust.* **26**(2), 2277 (1996)
4. C. Schulz, B.F. Kock, M. Hofmann, H. Michelsen, S. Will, B. Bougie, R. Suntz, G. Smallwood, *Appl. Phys. B* **83**(3), 333 (2006)
5. R.J. Santoro, H.G. Semerjian, *Symp. Int. Combust.* **20**(1), 997 (1985)
6. S. De Iulius, M. Barbini, S. Benecchi, F. Cignoli, G. Zizak, *Combust. Flame* **115**(1–2), 253 (1998)
7. A. D'Anna, A. Rolando, C. Allouis, P. Minutolo, A. D'Alessio, *Proc. Combust. Inst.* **30**(1), 1449 (2005)
8. M.D. Smooke, M.B. Long, B.C. Connelly, M.B. Colket, R.J. Hall, *Combust. Flame* **143**(4), 613 (2005)
9. O. Angrill, H. Geitlinger, T. Streibel, R. Suntz, H. Bockhorn, *Proc. Combust. Inst.* **28**(2), 2643 (2000)
10. H. Xu, F. Liu, S. Sun, Y. Zhao, S. Meng, W. Tang, *Combust. Flame* **177**, 67 (2017)
11. H. Jin, Y. Wang, K. Zhang, H. Guo, F. Qi, *Proc. Combust. Inst.* **34**(1), 779 (2013)
12. P.B. Kuhn, B. Ma, B.C. Connelly, M.D. Smooke, M.B. Long, *Proc. Combust. Inst.* **33**(1), 743 (2011)
13. D.D. Das, W.J. Cannella, C.S. McEnally, C.J. Mueller, L.D. Pfefferle, *Proc. Combust. Inst.* **36**(1), 871 (2017)
14. H. Liu, S. Zheng, H. Zhou, *IEEE Trans. Instrum. Meas.* **66**(2), 315 (2017)
15. R.L. Farrow, R.P. Lucht, W.L. Flower, R.E. Palmer, *Symp. Int. Combust.* **20**(1), 1307 (1985)
16. L.R. Boedeker, G.M. Dobbs, *Symp. Int. Combust.* **21**(1), 1097 (1988)
17. L.R. Boedeker, G.M. Dobbs, *Combust. Sci. Technol.* **46**(3–6), 301 (1986)
18. C.J. Klierer, Y. Gao, T. Seeger, J. Kiefer, B.D. Patterson, T.B. Settersten, *Proc. Combust. Inst.* **33**(1), 831 (2011)
19. D. Gu, Z. Sun, G.J. Nathan, P.R. Medwell, Z.T. Alwahabi, B.B. Dally, *Combust. Flame* **167**, 481 (2016)
20. Z. Sun, B. Dally, G. Nathan, Z. Alwahabi, *Combust. Flame* **175**, 270 (2017)
21. C. Liu, L. Xu, J. Chen, Z. Cao, Y. Lin, W. Cai, *Opt. Express* **23**(17), 22494 (2015)
22. C. Liu, L. Xu, F. Li, Z. Cao, S.A. Tsekenis, H. McCann, *Appl. Phys. B* **120**(3), 407 (2015)
23. Z. Qu, R. Ghorbani, D. Valiev, F.M. Schmidt, *Opt. Express* **23**(12), 16492 (2015)
24. G. Zhang, J. Liu, Z. Xu, Y. He, R. Kan, *Appl. Phys. B* **122**(1), 3 (2016)
25. L. Zhang, F. Wang, H. Zhang, J. Yan, K. Cen, *Chin. Opt. Lett.* **14**(11), 111201 (2016)

26. S. Wagner, M. Klein, T. Kathrotia, U. Riedel, T. Kissel, A. Dreizler, V. Ebert, *Appl. Phys. B* **109**(3), 533 (2012)
27. M.P. Esplin, R.J. Huppi, G.A. Vanasse, *Appl. Opt.* **21**(9), 1681 (1982)
28. S.P. Bharadwaj, M.F. Modest, *J. Quant. Spectrosc. Radiat. Transf.* **103**(1), 146 (2007)
29. T. Ren, M.F. Modest, A. Fateev, S. Clausen, *J. Quant. Spectrosc. Radiat. Transf.* **151**, 198 (2015)
30. V. Evseev, A. Fateev, S. Clausen, *J. Quant. Spectrosc. Radiat. Transf.* **113**(17), 2222 (2012)
31. R.M. Mihalcea, D.S. Baer, R.K. Hanson, *Appl. Opt.* **37**(36), 8341 (1998)
32. M.E. Webber, S. Kim, S.T. Sanders, D.S. Baer, R.K. Hanson, Y. Ikeda, *Appl. Opt.* **40**(6), 821 (2001)
33. K. Sun, R. Sur, X. Chao, J.B. Jeffries, R.K. Hanson, R.J. Pummill, K.J. Whitty, *Proc. Combust. Inst.* **34**(2), 3593 (2013)
34. R. Sur, K. Sun, J.B. Jeffries, R.K. Hanson, *Appl. Phys. B* **115**(1), 9 (2014)
35. R. Sur, K. Sun, J.B. Jeffries, J.G. Socha, R.K. Hanson, *Fuel* **150**, 102 (2015)
36. A. Klose, G. Ycas, F.C. Cruz, D.L. Maser, S.A. Diddams, *Appl. Phys. B* **122**(4), 1 (2016)
37. T. Cai, G. Gao, M. Wang, G. Wang, Y. Liu, X. Gao, *Appl. Phys. B* **118**(3), 471 (2015)
38. A. Farooq, J.B. Jeffries, R.K. Hanson, *Appl. Phys. B* **90**(3–4), 619 (2008)
39. A. Farooq, J.B. Jeffries, R.K. Hanson, *Appl. Opt.* **48**(35), 6740 (2009)
40. P. Nau, J. Koppmann, A. Lackner, K. Kohse-Höinghaus, A. Brockhinke, *Appl. Phys. B* **118**(3), 361 (2015)
41. R.M. Spearrin, W. Ren, J.B. Jeffries, R.K. Hanson, *Appl. Phys. B* **116**(4) 855 (2014)
42. R.M. Spearrin, C.S. Goldenstein, I.A. Schultz, J.B. Jeffries, R.K. Hanson, *Appl. Phys. B* **117**(2) 689 (2014)
43. K. Wu, F. Li, X. Cheng, Y. Yang, X. Lin, Y. Xia, *Appl. Phys. B* **117**(2), 659 (2014)
44. J.J. Girard, R.M. Spearrin, C.S. Goldenstein, R.K. Hanson, *Combust. Flame* **178**, 158 (2017)
45. L.H. Ma, L.Y. Lau, W. Ren, *Appl. Phys. B* **123**(3), 83 (2017)
46. R. Villarreal, P.L. Varghese, *Appl. Opt.* **44**(31), 6786 (2005)
47. S. Wagner, B.T. Fisher, J.W. Fleming, V. Ebert, *Proc. Combust. Inst.* **32**(1), 839 (2009)
48. J.A. Silver, D.J. Kane, P.S. Greenberg, *Appl. Opt.* **34**(15), 2787 (1995)
49. W. Cai, D.J. Ewing, L. Ma, *Comput. Phys. Commun.* **179**(4), 250 (2008)
50. P.E. Best, P.L. Chien, R.M. Carangelo, P.R. Solomon, M. Danchak, I. Ilovici, *Combust. Flame* **85**(3–4), 309 (1991)
51. D.R. Snelling, K.A. Thomson, G.J. Smallwood, Ö.L. Gülder, *Appl. Opt.* **38**(12), 2478 (1999)
52. S. Johnson, Faddeeva W function implementation. http://ab-initio.mit.edu/wiki/index.php/faddeeva_w. Accessed 13 Mar 2018
53. C.J. Dasch, *Appl. Opt.* **31**(8), 1146 (1992)
54. V. Dribinski, A. Ossadtchi, V.A. Mandelshtam, H. Reisler, *Rev. Sci. Instrum.* **73**(7), 2634 (2002)
55. Y. Zhang, C. Cao, Y. Li, W. Yuan, X. Yang, J. Yang, F. Qi, T.P. Huang, Y.Y. Lee, *Energy Fuels* **31**(12), 14270 (2017)
56. L.S. Rothman, I.E. Gordon, R.J. Barber, H. Dothe, R.R. Gamache, A. Goldman, V.I. Perevalov, S.A. Tashkun, J. Tennyson, *J. Quant. Spectrosc. Radiat. Transf.* **111**(15), 2139 (2010)
57. N.H. Ngo, D. Lisak, H. Tran, J.M. Hartmann, *J. Quant. Spectrosc. Radiat. Transf.* **129**, 89 (2013)